RSC Applied Interfaces

ROYAL SOCIETY OF CHEMISTRY

PAPER

View Article Online
View Journal

Cite this: DOI: 10.1039/d6lf00035e

Potentials of thin film silicon anodes in soft solid-state batteries

Julian Brokmann, *[ab] Han-Pin Hsieh, [c] Ann-Sophie Gail,[a] Matteo Kaminski,[ab] Nikolas Dilger,[a] Sebastian Melzig,[ab] Fu-Ming Wang [c] and Sabrina Zellmer[ab]

Received 5th February 2026,
Accepted 11th May 2026

DOI: 10.1039/d6lf00035e

rsc.li/RSCApplInter

Silicon is a promising anode material for solid-state batteries due to its high theoretical capacity, yet severe lithiation-induced volume changes lead to pronounced chemo-mechanical degradation at solid–solid interfaces. This work aims to identify a critical silicon thickness window that enables high reversible capacity while preserving mechanical integrity and interfacial stability in soft solid-state battery systems. By systematically varying the thickness of amorphous silicon thin-film anodes on copper current collectors, distinct thickness-dependent structure–property–performance relationships are revealed. Thin silicon films exhibit excellent cycling stability but limited capacity, whereas thicker films deliver high initial capacities followed by rapid degradation. An intermediate silicon thickness of approximately 500 nm provides the most favourable balance between reversible capacity and cycling stability. Post-cycling analyses link capacity decay at larger thicknesses to stress-driven cracking, delamination and electrical isolation of the silicon layer, consistent with mechanically induced failure during deep lithiation. These results demonstrate that the performance of silicon anodes in polymer-based solid-state batteries is governed by chemo-mechanical coupling and interfacial robustness rather than by active material loading alone. The findings provide practical design guidelines for thin-film silicon anodes in soft solid-state battery architectures.

1. Introduction

Solid-state batteries (SSBs) are being developed to achieve higher energy density and greater safety than conventional lithium-ion technology. Replacing the liquid phase with a solid ion conductor eliminates leakage and most solvent-driven parasitic reactions, extends the electrochemical stability window and allows the use of high-capacity anodes which would otherwise be difficult to integrate.[1–3] The core technical hurdles across electrolyte families are maintaining low interfacial resistance at practical stack pressures, securing chemo-mechanical compatibility during repeated cycling and achieving sufficient Li-ion conductivity at operating temperature.[3] Taken together, these interdependent challenges mean that the design of practical solid-state architectures is dominated by the electrode–electrolyte interface.[3]

Oxide, sulfide, halide, and polymer electrolytes represent distinct compromises. Dense oxides such as garnets offer wide anodic stability and chemical robustness, but they are stiff and brittle, often requiring elevated processing temperatures and externally applied pressures to sustain good interface contact.[4] Sulfides deliver liquid-like room-temperature conductivities and cold-press processability, yet their interfacial chemistry with layered oxide cathodes and highly reducing anodes demands careful passivation and moisture sensitivity complicates handling.[5,6] Halides occupy a middle ground with promising oxidative stability and improving transport, though their mechanics are still comparatively rigid.[7] In contrast, polymer and composite polymer electrolytes are mechanically compliant and can form conformal contact with textured electrodes at low pressure.[8,9] Their polymeric nature enables extensive chemical tunability through backbone design, salt selection and crosslinking,[9] as well as compatibility with scalable, roll-to-roll and solution-based fabrication routes.[10] It also allows for the deliberate design of composite architectures that stabilize electrode–electrolyte interfaces and improve long-term cycling stability.[1,2,11–13]

Polymer-based or more generally ‘soft-solid’ electrolytes are especially relevant where large anode strains must be

[a] Fraunhofer Institute for Surface Engineering and Thin Films IST, Riedenkamp 2, Braunschweig 38108, Germany. E-mail: sabrina.zellmer@ist.fraunhofer.de
[b] Technische Universität Braunschweig, Institute for Particle Technology, Volkmaroder Straße 5, Braunschweig 38104, Germany. E-mail: s.zellmer@tu-braunschweig.de
[c] Graduate Institute of Applied Science and Technology, National Taiwan University of Science and Technology, No.43 Keelung Rd., Sec. 4, Da'an Dist., Taipei City 106335, Taiwan, Republic of China. E-mail: mccabe@mail.ntust.edu.tw

accommodated. Ion transport in such media is coupled to polymer segmental motion and can be adjusted by backbone chemistry, side chains, cross-link density, the addition of plasticizers and the inclusion of ceramic fillers.[11] Ether-rich systems offer strong Li-salt solvation and decent mobility but have limited in oxidative stability. Composite approaches with nanofillers can raise modulus and suppress dendrite penetration while preserving percolating ion pathways. Just as important, soft electrolytes can act as binder-like interphases, wetting rough surfaces and redistributing stress during cycling. Reports on self-healing or dynamically cross-linked polymers show that the electrolyte can contribute to interface repair and contact retention under finite strain, a role that is inaccessible to brittle inorganic conductors.[11,14,15]

Among high-capacity anodes, silicon stands out due to its exceptionally high lithium storage capability. Depending on the assumed final composition, the theoretical gravimetric capacity is 3579 mAh g^{-1} for the $Li_{15}Si_4$ ($Li_{3.75}Si$) phase,[16] commonly regarded as the fully lithiated state at room temperature or up to 4200 mAh g^{-1} if the idealised stoichiometry of $Li_{4.4}Si$ is considered. In the $Li_{15}Si_4$ state, silicon exhibits a high volumetric capacity of approximately 2190 mAh cm^{-3} and a low operating potential *versus* Li/Li^+ of below 0.4 V.[16] Furthermore, it is based on an earth-abundant element.[17] However, the lithium-alloying mechanism, which accommodates up to 3.75 lithium atoms per silicon atom, is accompanied by a pronounced volume expansion of over 300% during lithiation and delithiation.[18] This large, repeated dimensional change induces substantial mechanical stresses, which can ultimately lead to the electrode's structural degradation and progressive capacity fading. A theoretical gravimetric capacity of 3579 mAh g^{-1} is therefore used as the reference value for silicon, as this represents the fully lithiated state that is practically relevant under typical room-temperature cycling conditions.[17] To meet the challenges, in addition to SiO_x[19] or Si/C[20] anodes with various silicon structures[21] like nanoparticles,[22] hollow structures,[23] nanotubes[24] and pure Si metal anodes[25] are used. This can further increase the gravimetric energy density in solid-state battery cells and reduce the absolute layer expansion of the anode due to the possibility of significantly lower layer thicknesses. By utilizing this approach, it is possible to reduce the incidence of detachment and subsequent contact loss. To realize pure silicon anodes the utilization of multiple processes, such as silicon alloying[26] or silicon microfabrication[27] can be used to produce high purity silicon layers with tailored properties.

In liquid cells the resulting pulverization, continuous SEI growth, and loss of electronic percolation are well documented.[17] In solid-state cells, the failure modes concentrate at the solid–solid interface: debonding, interfacial voiding, and the growth of resistive reaction layers amplify impedance growth and accelerate capacity fade if not actively managed.[1–3,17] Polymer electrolytes mitigate a part of this problem by providing compliance and wetting. Nevertheless they cannot by themselves eliminate the fundamental strain mismatch when the anode is thick or structurally heterogeneous.[11,14] The practical conclusion from the literature is to reduce absolute silicon thickness, control its amorphous structure to avoid sharp two-phase transitions, and tailor the interface so that the electrolyte can deform with the anode while remaining ionically conductive and electronically insulating.

Thin-film silicon electrodes are well suited to implement and study this strategy. Physical vapor deposition enables ultrathin, high-purity amorphous Si layers with good thickness control and very low porosity.[28] At sufficiently low thickness, absolute strain is reduced and the film can expand predominantly through thickness rather than laterally, which lowers stress intensity at the current collector and the electrolyte interface. Thin-film studies in liquid electrolytes already established the thickness-lifetime trade-off, with tens of nanometers films (down to 50 nm) sustaining high reversible capacity for hundreds of cycles.[17,28] More recent soft-solid reports extend this concept by integrating compliant polymer electrolytes. Silicon should be maintained in an ultrathin, predominantly amorphous form, with robust adhesion to a ductile current collector. In addition, the polymer electrolyte must provide sufficient ionic conductivity and mechanical stiffness at the operating temperature, while the lithium inventory and anode–electrolyte interfacial chemistry are controlled from the initial electrochemical cycles onward.[11,17,28–30]

2. Experimental section

Within this framework conditions, the present work evaluates sputtered thin-film silicon on copper current collectors in soft-solid configurations using a polysiloxane- and methacrylate-based polymer electrolyte. The focus is on the interaction between film thickness, morphology, and interfacial impedance in half-cells as well as the resulting capacity retention at elevated temperature where polymer transport is favourable. The approach is deliberately minimalist in electrode architecture to expose rate-limiting phenomena at the silicon–electrolyte and silicon–collector interfaces. Previous studies have shown that, even in seemingly simple thin-film silicon model systems, the electrochemical performance cannot be separated from the effects induced by mechanical forces at the silicon–current collector interface, especially when rigid metallic substrates are used.[31] By combining controlled deposition and systematic thickness variation, the aim was to map a practical thickness window for soft-solid operation and to extract structure–property relations that are transferable to higher-loading architectures. Iaboni and Obrovac provided an important mechanistic perspective on silicon thin-film anodes, showing that the electrochemical behaviour of sputtered silicon films is strongly affected by mechanical stresses arising from their bonding to metallic current collectors, particularly copper.[31] During lithiation, the

significant volume expansion of silicon generates compressive stresses that directly impact the electrode potential, shifting the lithiation voltage towards lower values.[32] With continued cycling, stress can be partially relieved through plastic deformation, crack formation or local interfacial debonding, thereby changing the mechanical properties of the silicon layer.[31] These considerations emphasize the importance of film thickness, adhesion to the copper current collector and the mechanical properties of the surrounding electrolyte in the design of sputtered silicon thin-film electrodes.

In soft solid-state battery systems employing polymer electrolytes, it has been demonstrated that there is the possibility of maintaining conformal contact with the electrode and accommodating mechanical deformation to a certain extent, while the underlying substrate constraint remains unchanged. Consequently, coupled electro-chemo-mechanical effects must be explicitly considered when analysing interfacial stability and long-term cell performance.

Thin-film silicon deposition by DC magnetron sputtering

Thin-film silicon electrodes were prepared using DC magnetron sputtering (see Fig. 1) to enable precise control of the film thickness and consistent deposition conditions. As illustrated in Fig. 1a, the process chamber is operated in a bottom-up configuration, with the silicon target mounted in a crucible on the generator cathode and the copper foil substrate fixed to the upper substrate plate. The argon process gas is introduced from below, while evacuation is achieved *via* an oil diffusion pump connected to the chamber. Fig. 1b shows the top-down view of the circular magnetron geometry, highlighting the concentric magnetic field arrangement that confines the plasma above the target surface. The resulting plasma localisation, schematically indicated by the curved ion trajectories, ensures efficient sputtering of silicon while limiting direct plasma exposure of the substrate. Prior to deposition, the chamber was evacuated to a base pressure of approximately 4×10^{-6} mbar to minimize residual gas contamination. High-purity argon (5.0) was used as the sputtering gas at a flow rate of 12.5 Sccm, resulting in a working pressure of approximately 1.5×10^{-2} mbar. Silicon was deposited from a high-purity silicon target (99.999%) bonded to a copper backing plate using a silver-filled epoxy adhesive. The circular target had a diameter of 90 mm, a thickness of 7 mm and a central bore of 6 mm. Sputtering was carried out with a MDX 500 generator from Advanced Energy (USA) at a constant DC power of 350 W and prior to deposition the target was pre-sputtered for 25 minutes with the substrate shielded, in order to remove surface contamination and stabilize the plasma. Depositions were performed onto cold-rolled copper foil substrates without active substrate heating. The target-to-substrate distance was fixed at 21 cm and a bottom-up configuration was employed, with the target positioned below the substrate holder. No external substrate bias was applied, and all films were deposited continuously without plasma interruption. Under these conditions, a deposition rate of approximately 12 nm min^{-1} (2 Å s^{-1}) was obtained, as monitored *in situ* by a quartz crystal microbalance. Film thicknesses were subsequently calibrated *ex situ* using profilometry.

Soft-solid polymer electrolyte synthesis

The soft-solid polymer electrolyte was prepared by a platinum-catalyzed hydrosilylation reaction using poly(ethylene glycol) methyl ether methacrylate (PEGMEMA, Mn = 950), poly(methylhydro)siloxane (PMHS), and 2-carboxyethyl acrylate (CEA). PEGMEMA (0.0135 mol), PMHS (0.0165 mol), CEA (0.0015 mol), and 8 μL of a platinum catalyst were dissolved in 150 mL tetrahydrofuran (THF) in a three-necked flask equipped with a reflux condenser. The reaction mixture was heated to 80 °C and kept under reflux

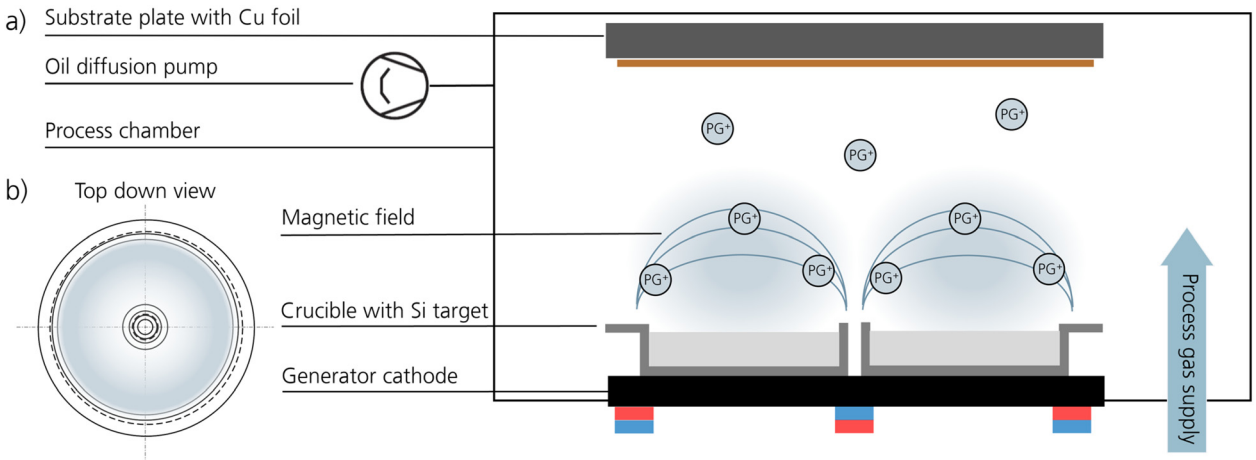

Fig. 1 (a) Schematic diagram of the bottom-up magnetron sputtering system used, (b) with top-down view of the round crucible with silicon target.

for 72 h.[32] After this step, lithium hydroxide was added to convert the carboxylic acid groups into their lithium form, yielding a pre-lithiated polymer network. The reaction was continued for another 24 h under the same conditions. The solvent was then removed under reduced pressure, and the residue was washed with *n*-hexane to remove unreacted monomers. The resulting polymer was referred to as CEAM950.[33–35] The final material is a solvent-free, soft-solid polymer electrolyte suitable for use in solid-state cells.

Cell assembly and electrochemical characterization

Electrochemical test cells were assembled in CR2032 coin cell cases, using sputtered silicon-on-copper (Si@Cu) anodes with a diameter of 14 mm. The half-cells were configured with lithium-on-copper foil as the counter and reference electrode with a diameter of 16 mm. All cell assembly steps were carried out in an argon-filled glovebox. A polyethylene separator with a thickness of 12 μm was pre-immersed in the soft-solid polymer electrolyte for over 1 hour prior to assembly and was then placed between the anode and the counter electrode. The stacking sequence in the coin cell was as follows: Si@Cu anode |electrolyte-impregnated separator| Li-on-Cu counter electrode. Stainless steel spacers with a total thickness of 1.7 mm were placed between the counter electrode and the wave spring to define the stack height and ensure consistent compression. A stainless-steel wave spring was used to maintain stable contact under compression. The cells were sealed and crimped at 800 psi, which corresponds to an applied pressure of approximately 5.5 MPa. Electrochemical testing was performed using a BasyTec CTS battery test system. All electrochemical measurements were conducted at 60 °C to ensure sufficient ionic conductivity of the polymer electrolyte and to minimize transport limitations. At room temperature, the low ionic conductivity ($\approx 10^{-6}$–10^{-7} S cm^{-1}) would lead to pronounced polarization, obscuring thickness-dependent interfacial effects. The half-cells were cycled within a voltage window of 1.0–0.01 V *versus* Li/Li$^+$. Lithiation was carried out in constant-current–constant-voltage (CCCV) mode at a C/20 rate up to 1.0 V (CC), followed by a constant-voltage step until the current dropped below 0.005 C and delithiation was performed galvanostatically at a C/20 rate down to 0.01 V. C-Rates were defined with respect to the theoretical gravimetric capacity of silicon (~3579 mAh g_{Si}^{-1}). A current rate of C/20 was selected to minimize kinetic and transport limitations and to enable a focus on intrinsic thickness-dependent chemo-mechanical processes in silicon films.

The electrodes were cycled at a constant C-rate rather than a constant current density. This approach allows for a comparable lithiation rate per unit mass of active material across all layer thicknesses. The goal was to achieve a more meaningful comparison of the intrinsic, thickness-dependent chemical–mechanical and transport processes.

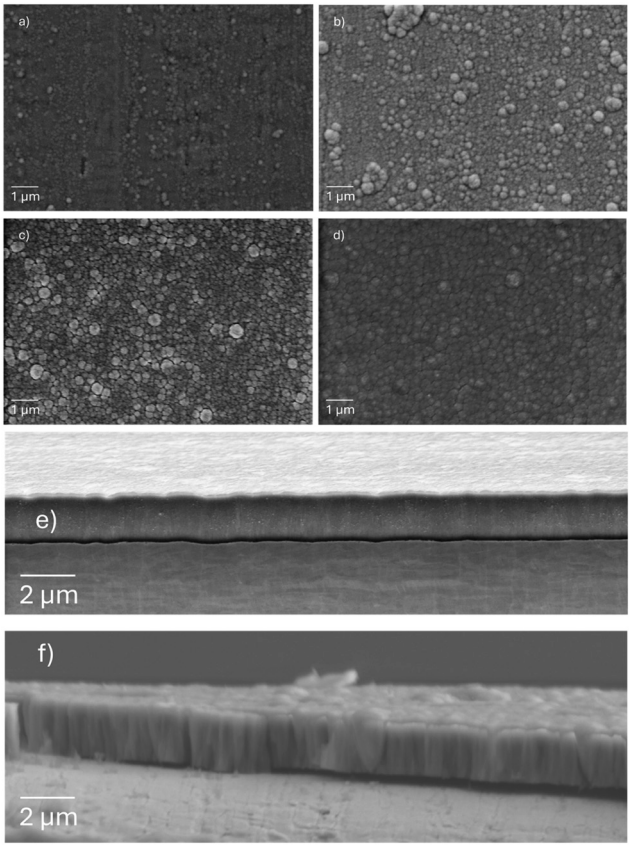

Fig. 2 Scanning electron microscope (SEM) images of the surface of a silicon on copper anode with a 10 000× magnification and a layer thickness of (a) 200 nm, (b) 500 nm, (c) 1000 nm, (d) 2000 nm, (e) SEM image of an ion mill cross-section of a 2 μm silicon on copper anode with a 5000× magnification, (f) SEM image of a fracture edge of a 1 μm silicon on copper anode with a 10 000× magnification.

3. Results and discussion

Morphological and structural characterization

To investigate the properties of magnetron-sputtered silicon on copper, surface images were recorded at different magnifications using scanning electron microscopy. The growth behaviour of silicon during sputtering is strongly governed by the properties of the substrate. The 10 μm thick copper foil used in this study was produced by cold rolling, which introduces a pronounced preferential direction that propagates into the silicon layer and significantly influences the nucleation behaviour, as visible in Fig. 2a. The growth mode of PVD-deposited films can be described by Thornton's structural zone model,[36] which relates film morphology to the sputtering gas pressure and the ratio of substrate temperature to the melting temperature of the deposited material, T_S/T_m. Under the deposition conditions applied here, characterized by low sputtering gas pressure and a low T_S/T_m ratio, silicon growth is expected to occur in zone 1. In this regime, surface diffusion is strongly limited, such that the evolving film largely replicates the topography of the substrate. In addition, shadowing effects between individual

columnar structures restrict the formation of new nucleation sites, resulting in a limited number of growth centers and the development of a rough and irregular surface texture, particularly for thicker layers (Fig. 2b–d). As a result, the surface and cross-sectional SEM images reveal a pronounced thickness-dependent evolution of morphology, mechanical integrity, and growth behaviour of the silicon layers. At a thickness of 200 nm, the Si surface appears smooth and compact with a fine granular texture, consistent with a dense initial growth regime dominated by island formation and the early stages of film densification (see Fig. 2a). At 500 nm, the surface morphology becomes rougher and more heterogeneous, reflecting continued columnar growth and progressive domain growth typical for amorphous silicon deposited by physical vapor deposition,[36,37] while localized narrow discontinuities indicate the beginning of tensile stress accumulation as the growing film becomes increasingly constrained by the copper substrate (see Fig. 2b). At a thickness of 1000 nm, a continuous crack network develops, separating the surface into well-defined domains and indicating stress-driven segmentation of vertically extended growth domains (see Fig. 2c). For the 2000 nm Si layer, this segmentation is strongly pronounced, with wide and continuous crack boundaries, large domains, and local surface lifting, suggesting that stress relaxation increasingly proceeds through fracture and partial delamination rather than elastic accommodation within the film (see Fig. 2d). The cross-sectional SEM images support this interpretation (see Fig. 2e). The ion-milled cross section of the 2 μm Si@Cu electrode shows a continuous silicon layer with a sharp interface to the copper substrate and distinct through-thickness contrast variations, consistent with a columnar or segmented internal growth structure extending from the interface toward the surface. A locally observed dark contrast region near the Si–Cu interface suggests interfacial weakening, potentially arising from stress concentration during growth. The fracture-edge image of the 1000 nm Si layer exhibits a stepped, vertically structured fracture surface, further supporting a columnar growth morphology and brittle fracture behaviour through the film thickness (see Fig. 2f). Taken together, these observations demonstrate a transition from dense, substrate-replicating growth at low thickness to columnar, stress-dominated growth at higher thicknesses, accompanied by mechanical segmentation and reduced structural integrity of the silicon layer on copper.

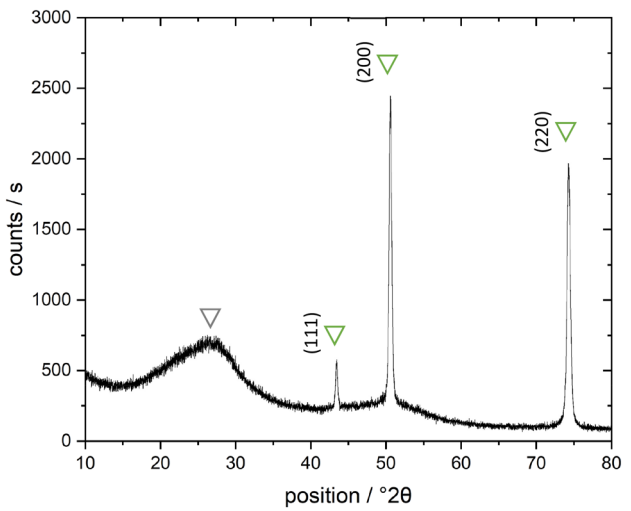

Fig. 3 X-ray diffraction (XRD) pattern of a magnetron-sputtered silicon thin film deposited on a copper substrate. The diffractogram is dominated by reflections from the Cu substrate ((111), (200), (220)). A broad feature in the range of 20–35° with a maximum around 27–28° indicates the presence of amorphous phases, which are attributed to a mixture of amorphous Si and SiO_X. The presence of oxygen in the films is confirmed by EPMA (Table S1). No crystalline silicon or silicon oxide phases are detected.

Fig. 3 shows the X-ray diffraction (XRD) pattern of a silicon layer deposited by magnetron sputtering on a copper substrate, recorded in the 2θ range from approximately 10° to 80°. The diffractogram is dominated by sharp reflections at around 43°, 50°, and 74°, corresponding to the Cu (111), (200) and (220) planes, indicating the high crystallinity and texture of the copper substrate. A broad, low-intensity feature is observed in the range of approximately 20–35° with a maximum at around 27–28°, which is characteristic of amorphous phases. This feature cannot be attributed exclusively to amorphous silicon but is instead consistent with a combination of amorphous Si and SiO_X. The presence of oxygen in the films is confirmed by electron probe microanalysis (EPMA, Table S1), which reveals a substantial oxygen fraction for all investigated thicknesses. This indicates that the deposited layers are more accurately described as amorphous Si–O_X mixtures rather than pure amorphous silicon with a thin surface oxide. Due to the amorphous nature of both Si and SiO_X, a clear separation or phase quantification by XRD is not possible. No distinct crystalline oxide phases are detected, suggesting that the oxygen-containing phases are amorphous. The absence of sharp silicon Bragg reflections confirms that the deposited silicon is predominantly amorphous,[38] consistent with growth in Thornton zone 1 under limited surface diffusion conditions.

XRD analysis after lithiation (Fig. S2, 10–80°, 2θ) reveals a broad amorphous halo associated with Li_XSi, while the diffractogram is dominated by reflections from the Cu current collector. No distinct peaks attributable to crystalline lithium silicide phases, such as $Li_{15}Si_4$, are observed within the measured angular range, indicating that the silicon remains predominantly amorphous after lithiation.

Fig. 4 combines a cross-sectional SEM image with an EDX line scan across a Si@Cu stack. The SEM micrograph (bottom) shows the cross section and the scan path (yellow line). The corresponding EDX profiles (top) plot the relative intensities of Cu, Si, and O along the scan distance. A pronounced Si signal is detected in the central region, while the Cu signal is strongly reduced there and rises sharply toward the Cu-rich regions. Oxygen shows a finite signal

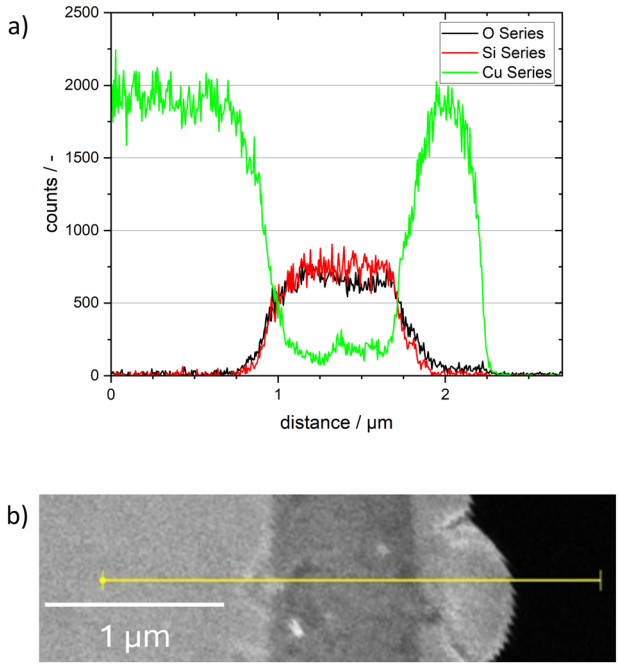

Fig. 4 Combined SEM-EDX line-scan analysis of a Si layer on a Cu substrate. (a) The upper panel shows the line profiles of Cu, Si, and O recorded through the cross section. A strong Si signal is observed in the central area, accompanied by a low O contribution, while the Cu signal is strongly suppressed in this area and increases sharply toward both sides, consistent with the underlying Cu substrate. (b) The lower panel displays the corresponding ion-milled cross-sectional SEM image, with the yellow line indicating the position of the EDX line scan.

within the Si-dominated region and decreases toward the Cu-rich areas. The anti-correlated Si and Cu profiles confirm a chemically distinct Si layer on Cu with a comparatively sharp transition on the micrometre scale. The oxygen contribution within the Si region is consistent with partial oxidation of the silicon during preparation. Importantly, the elevated Cu signal detected 'above' the Si-rich region should not be interpreted as an additional Cu layer in the original sample. It is an artefact caused by ion milling from the copper side: material removed during milling is redeposited and forms a superficial Cu-containing layer on top of the silicon.

In the context of the previous SEM and XRD results, the EDX line scan adds chemical evidence that the sputtered Si film remains compositionally separated from the Cu substrate, consistent with the XRD indication of amorphous Si on crystalline Cu. The absence of a broad intermixing zone supports the view that the thickness-dependent cracking and segmentation observed in SEM are governed primarily by stress evolution and growth morphology rather than by extensive Cu–Si interdiffusion. At the same time, the detected oxygen within the Si region fits well with the atmosphere-based preparation route and should be considered when interpreting near-surface signals, particularly in regions affected by cracking or high surface roughness.

Electrochemical and mechanical properties of the CEAM950 polymer electrolyte

The electrochemical properties of the CEAM950 polymer electrolyte were evaluated under the same conditions as the electrochemical testing of the half cells, *i.e.* at 60 °C. This elevated temperature is required to ensure sufficient ionic transport in polymer-based solid electrolytes and is consistent with previous reports on solvent-free polymer systems.[8,39,40] The ionic conductivity was determined by electrochemical impedance spectroscopy using a stainless-steel blocking electrode configuration. At 60 °C, the ionic conductivity reaches 3.41×10^{-5} S cm^{-1}, which lies within the typical range reported for polymer electrolytes without additional liquid plasticizers or high salt loading. In such systems, ionic conductivity at room temperature is generally reduced by one to two orders of magnitude due to segmental motion limitations of the polymer chains.[39,40] Since all electrochemical measurements in this study were conducted at 60 °C, room-temperature performance is not relevant for the conclusions drawn here.

The electrochemical stability window was evaluated by linear sweep voltammetry at 60 °C with a scan rate of 1 mV s^{-1} between 0 and 5 V *vs.* Li/Li$^+$ (see S1). The current response remains at a very low level over the entire voltage range, indicating the absence of significant oxidative decomposition under these conditions. It should be noted that LSV provides a qualitative estimate of oxidative stability and the exact onset potential depends on the chosen current threshold and electrode configuration. Nevertheless, the results confirm sufficient stability for the voltage range applied in this study. Regarding mechanical properties, CEAM950 is a highly compliant polymer electrolyte. Due to its soft, viscoelastic nature, conventional determination of a well-defined Young's modulus is challenging. Instead, such materials are typically characterized by low effective moduli in the MPa or sub-MPa range, several orders of magnitude lower than those of inorganic solid electrolytes such as oxides or sulfides.[41,42] This low stiffness enables efficient stress relaxation at the electrode–electrolyte interface and is a key factor in accommodating the large volume changes of silicon during cycling. Overall, the combination of moderate ionic conductivity at elevated temperature, sufficient electrochemical stability, and pronounced mechanical compliance supports the classification of the system as a soft solid-state battery and explains the improved chemo-mechanical stability observed.

Electrochemical performance

Considering the moderate ionic conductivity at 60 °C and the pronounced mechanical compliance of the polymer electrolyte discussed above, the electrochemical response of the Si@Cu electrodes must be interpreted as a coupled transport-mechanical problem. Fig. 5a shows the electrochemical impedance spectroscopy of a silicon anode with 200 nm of silicon on copper, which corresponds with an

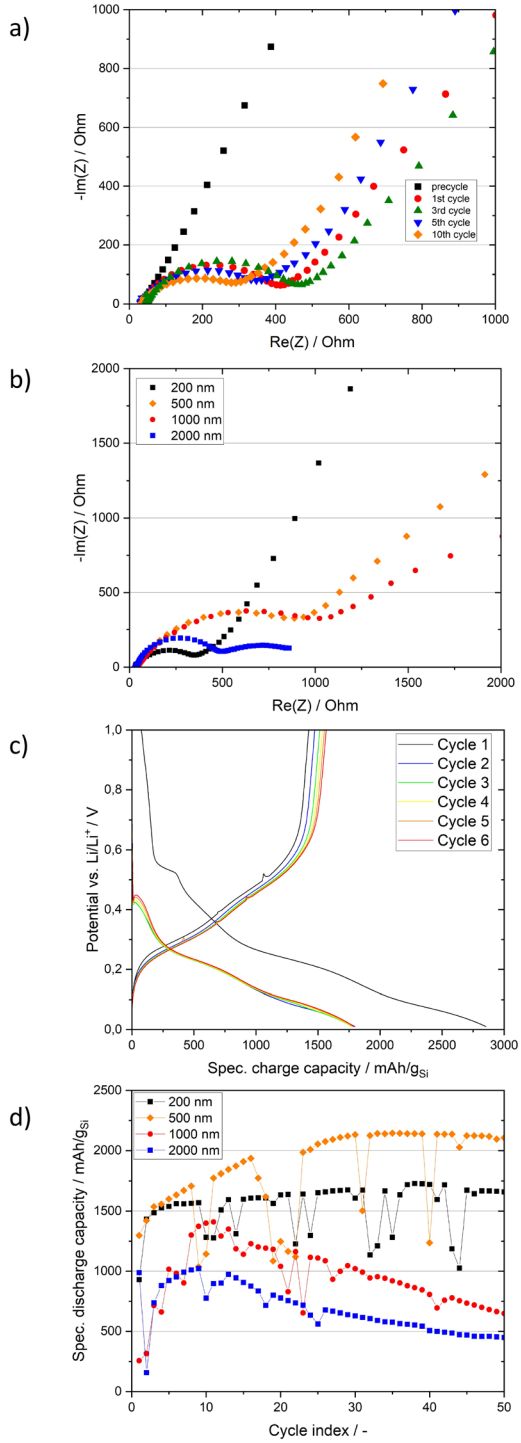

Fig. 5 (a) Electrochemical impedance spectroscopy of an anode with 200 nm silicon on copper precycle and after 1, 3, 5 and 10 cycles (b) electrochemical impedance spectroscopy of anodes with 200 nm, 500 nm, 1000 nm and 2000 nm silicon on copper after 5th cycle (c) cycling result of a 200 nm silicon on copper anode in a half-cell test against lithium metal (d) comparison of the specific discharge capacities in the first cycles of a 200 nm, 500 nm, 1000 nm and 2000 nm silicon on copper anode in a half-cell test against lithium metal.

areal loading of 0.0394 mg cm^{-2}. This value lies within the typical range reported for sputtered silicon thin-film anodes, as demonstrated in previous studies.[43] The pre-cycle Nyquist response reveals a small semicircle at very low Z, this is consistent with an initially well-contacted silicon–polymer interface and low interfacial resistance in a soft ether-siloxane–acrylate matrix.[44,45] After the first cycle, the spectrum expands, a distinct mid-frequency arc emerges, and a lengthening low-frequency tail appears. This evolution is consistent with the formation of a polymer-derived interphase.[46] These are electronically insulating and only moderately ionically conductive. Simultaneously, chemo-mechanical expansion of amorphous silicon increases the roughness of the interface. Across subsequent cycles (3rd–10th), the continued growth of the mid-frequency arc and increasingly diffusive tail could indicate thickening and structuring of the surface. In addition, the moderate ionic conductivity of the polymer electrolyte contributes to the pronounced transport limitations, particularly as the effective diffusion length increases with film thickness.

Fig. 5b shows that an increase of the Si layer thickness from 200 nm to 1000 nm results in a monotonic increase in total impedance, as indicated by broader semicircles and an extended low-frequency tail. This is consistent with prior observations that thicker Si films display higher resistance and poorer electrochemical utilisation under comparable conditions.[47] The spectra can be explained by transport geometry, thicker films lead to an increase of the characteristic Li^+ diffusion length, causing the electrode to show more prominent (finite-length) Warburg diffusion behaviour. Consequently, the apparent mid-frequency arc increases in size and the low-frequency tail becomes longer in the Nyquist plot. This is consistent with the standard descriptions of impedance spectroscopy of diffusion in thin films. Amorphous Si accumulates substantial cyclic stresses during (de)lithiation. Thicker films store more elastic/plastic energy and are more prone to cracking and interfacial delamination. This reduces the real contact area and raises the effective interfacial/constriction resistance, which contributes to the mid-frequency arc.[48] In soft polymer solid electrolytes, this trend can be even stronger. The softness of the polymer electrolyte, *i.e.* its low effective modulus in the MPa or sub-MPa range, only transiently mitigates contact defects. Although its low modulus promotes excellent initial contacting and a small pre-cycle arc, viscoelastic creep and stress relaxation gradually dissipate stack pressure at the silicon-electrolyte interface. During cycling, amorphous silicon expands and contracts. In a polymeric, mechanically compliant medium, interfacial degradation is partially mitigated through deformation accommodation, yet elastic recovery during discharge remains incomplete, leading to residual interfacial voids. Simultaneously, the polymer-derived interphase, while mechanically soft, exhibits only moderate ionic conductivity and progressively thickens, thereby increasing interfacial resistance.[49] The combined effects of creep-driven pressure decay, interphase build-up and low shear

stiffness create the same impedance signatures as for thicker silicon films. Overall, thin silicon exhibits smaller arcing and lower diffusion limitations, as stresses are reduced and Li^+ access is improved. These trends are consistent with the known interaction between transport length scales, fracture and interface quality in silicon anodes.[48] Up to a thickness of 1000 nm, the impedance response follows this trend.

The 2000 nm Si@Cu electrode, on the other hand, deviates significantly from the expected trend: instead of higher impedance and a more diffusion-controlled reaction, the Nyquist spectrum appears compressed and does not show the expected broadening of the low-frequency range. This suggests that, at this thickness, the electrode is no longer homogeneously electrochemically active, but rather that only a few effective transport pathways or a reduced, electrically poorly connected volume dominate the measured impedance. Taken together, the impedance spectra indicate a transition from predominantly capacitive interfacial behaviour with increasing diffusion contributions at intermediate thicknesses, to a regime in which the electrochemical response is governed by localized transport processes. The underlying structural origin of this transition is addressed in the post-mortem analysis discussed below. Equivalent circuit fits are provided in the SI (see Fig. S4).

Fig. 5c shows the galvanostatic voltage-capacity curves for the first six cycles of a cell employing a 1 μm sputtered silicon film on copper. Initial lithiation in cycle 1 exhibits the characteristic downward slope below approximately 0.1 V, which is associated with lithium alloying in amorphous silicon.[16] The corresponding delithiation proceeds through a broad feature around 0.4–0.5 V and shows pronounced voltage hysteresis relative to lithiation, indicating significant kinetic and transport polarisation during the initial formation stage. From cycle 2 onwards, the charge and discharge curves move closer together and largely overlap, reflecting partial stabilisation of the interphase and a more reproducible electrochemical contact at the silicon–polymer electrolyte interface after formation. Despite the reduction in hysteresis, the accessible capacity during lithiation and delithiation decreases from cycle 1 to cycle 6. This behaviour is consistent with an early loss of electrochemically active volume due to interphase growth, as well as chemo-mechanical degradation that is amplified at a film thickness of 1 μm.[16,45] The evolution of the curve shape is indicative of a progressive limitation of lithiation to regions close to the interface. The persistent low-voltage slope during lithiation, together with the comparatively flatter delithiation profile, suggests increasing transport limitations through the developing interphase and the lithiated silicon. Contact heterogeneity induced by microcrack formation raises the overpotential and further restricts the utilization of the film. By cycle 6, the voltage-capacity profiles become reproducible and comparatively narrow, indicating that a new steady state has been reached. In this steady state a thin, electrochemically well-connected fraction of the silicon continues to cycle, while the bulk of the material contributes less to the overall capacity.[16]

Fig. 5d compares the specific discharge capacities of Si@Cu half cells with silicon layer thicknesses of 200 nm, 500 nm, 1000 nm and 2000 nm over 50 galvanostatic cycles. The results reveal a clear dependence of both achievable capacity and cycling stability on thickness. The 200 nm silicon electrode delivers a moderate initial capacity but demonstrates the greatest stability with minimal capacity decay upon repeated cycling. Increasing the silicon thickness to 500 nm (0.0985 mg_{Si} cm^{-2}) substantially increases the accessible capacity, which remains stable over a significant number of cycles. By contrast, electrodes with 1000 nm (0.197 mg_{Si} cm^{-2}) and 2000 nm-thick Si layers demonstrate very high initial capacities, followed by rapid capacity fading and poor long-term stability. The initial increase in capacity observed for all electrodes is attributed to a progressive improvement of the interfacial contact between the silicon film and the polymer electrolyte. In contrast to liquid electrolyte systems, where wetting is immediate, the soft solid-state configuration initially exhibits limited ionic contact. During cycling, mechanical adaptation of the polymer electrolyte and structural evolution of the silicon film enhance the effective contact area and facilitate lithium transport into previously less accessible regions. This results in a gradual activation of the electrode and an increase in accessible capacity. This interpretation is supported by the evolution of the impedance spectra, which indicates changes in interfacial and transport properties during the initial cycles. Stack pressure is known to influence interfacial contact and mechanical stabilization in solid-state batteries.[50] In the present coin cell configuration, the applied pressure is defined by the cell assembly and was kept constant across all experiments.

These electrochemical trends are consistent with the morphological and structural characteristics of the sputtered silicon films discussed previously[51,52] and can be further rationalized in the context of the work by Iaboni *et al.*,[53] who investigated the mechanical stability of thin-film silicon electrodes as a function of thickness. They identified a critical thickness for amorphous silicon films, beyond which lithiation-induced stresses can no longer be elastically accommodated, leading to cracking, segmentation and progressive electrical isolation of the active material.

Ex situ XRD measurements performed on lithiated silicon electrodes did not reveal any distinct diffraction peaks attributable to crystalline $Li_{15}Si_4$, indicating that the silicon remains predominantly amorphous under the applied conditions. Within the resolution of the present measurements, no evidence for crystalline phase formation is observed. Consequently, the degradation behaviour discussed here is attributed to stress evolution within amorphous Li_xSi in combination with morphological factors such as columnar growth and crack propagation.

In this framework, the stable cycling behaviour of the 200 nm silicon electrode can be attributed to its dense,

largely crack-free morphology and the fact that its thickness is well below the critical fracture threshold identified by Iaboni *et al.* Most of the silicon remains mechanically intact and electronically connected, resulting in good capacity retention despite the limited amount of active material available. The 500 nm Si layer occupies an intermediate regime close to the critical thickness reported for sputtered amorphous silicon films. At this thickness, a substantially larger active volume is available compared to thinner films, while mechanical degradation such as crack formation and segmentation remains sufficiently limited to preserve electronic connectivity over a large fraction of the film. This balance between active material utilisation and mechanical integrity enables the 500 nm electrode to achieve the highest reversible capacities with acceptable cycling stability. For thicknesses of 1000 nm and 2000 nm (0.394 mg_{Si} cm^{-2}), the mechanically unstable regime described by Iaboni *et al.* becomes dominant. Deeper lithiation increases the degree of volume expansion within amorphous Li_xSi, leading to pronounced stress accumulation. In combination with the columnar growth morphology observed in SEM, this promotes crack formation, fragmentation and interfacial degradation. Consequently, large portions of the Si layer become electrically disconnected and lithiation becomes increasingly confined to regions near the Si–Cu interface, leading to rapid capacity decay despite the higher nominal Si loading.

Overall, the half-cell results, together with the morphological and structural analyses, suggest that an optimal thickness window exists for thin-film Si anodes. Below this window, capacity is limited by active mass, whereas above it mechanical fracture and electrical isolation dominate.[54] In the present system, a silicon thickness of around 500 nm is close to this optimum, providing the best balance between high reversible capacity and sustained electrochemical stability.

The observed optimum at around 500 nm suggests a balance between capacity and degradation mechanisms. To contextualize the observed thickness-dependent behaviour, it is instructive to compare the present results with previous studies on Si thin-film anodes in liquid electrolyte systems. In such systems, an optimal thickness is typically reported in the sub-micrometre range, reflecting a trade-off between areal capacity and increasing limitations from Li transport, mechanical stress accumulation and unstable solid electrolyte interphase formation, as demonstrated for model Si systems in liquid electrolytes (*e.g.* Sethuraman *et al.*,[48] McDowell *et al.*[18] and Ryu *et al.*[55]). While our results similarly indicate a performance maximum at intermediate thickness (~500 nm), the underlying mechanisms are expected to differ in solid-state configurations. In the absence of a liquid electrolyte and continuous interphase reformation, interfacial kinetics and chemo-mechanical constraints are governed by the solid electrolyte and its contact with the Si layer. This may mitigate some of the parasitic effects typically observed in liquid systems, while introducing additional limitations related to interfacial contact loss and constrained volume expansion. Therefore, the thickness optimum identified here cannot be directly transferred from liquid electrolyte studies, but instead reflects the specific interplay of transport and mechanical effects in the solid-state system.

Post-mortem analysis

Fig. 6 show optical post-mortem images of the Si@Cu half cells after 50 galvanostatic cycles at C/20, that reveal macroscopic integrity and adhesion depend significantly on silicon layer thickness. The 200 nm Si@Cu electrode retains an intact and continuous appearance, with the silicon film uniformly covering the copper substrate with no evidence of delamination. Only minor discoloration is observed, which can be attributed to electrolyte residues and surface reactions during cycling. This behaviour is consistent with the stable electrochemical performance and the dense, crack-free morphology observed prior to cycling, indicating that lithiation-induced stresses remain below the critical threshold for interfacial failure at this thickness, in line with the concept of a critical dimension for mechanically stable silicon electrodes.[53,54,56]

For the 500 nm Si@Cu electrode, optical imaging reveals partial discoloration and localized regions of delamination, while large areas of the silicon film remain adhered to the copper substrate. This intermediate degradation state is consistent with the onset of stress-driven cracking and segmentation observed in SEM prior to cycling, indicating that local elastic accommodation is exceeded during repeated volume changes. However, the incomplete delamination suggests that a substantial fraction of the silicon remains mechanically and electronically connected, enabling sustained electrochemical activity. Similar behaviour has been reported for amorphous silicon films near their critical thickness.[48] In contrast, severe macroscopic degradation is observed for the 1000 nm and 2000 nm Si@Cu electrodes. Extensive delamination, fragmentation and near-complete detachment of the silicon layers are evident, correlating with rapid capacity fading and pronounced crack networks

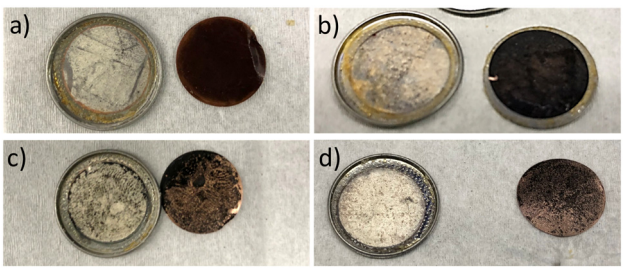

Fig. 6 Optical photographs of Si-coated Cu electrodes with increasing Si thickness after electrochemical cycling. From left to right, the samples correspond to (a) 200 nm, (b) 500 nm, (c) 1000 nm and (d) 2000 nm Si deposited on Cu. The images show post-mortem half cells that were disassembled after 50 galvanostatic cycles at C/20, illustrating the different adhesion states of the Si layers on the Cu substrates as a function of film thickness.

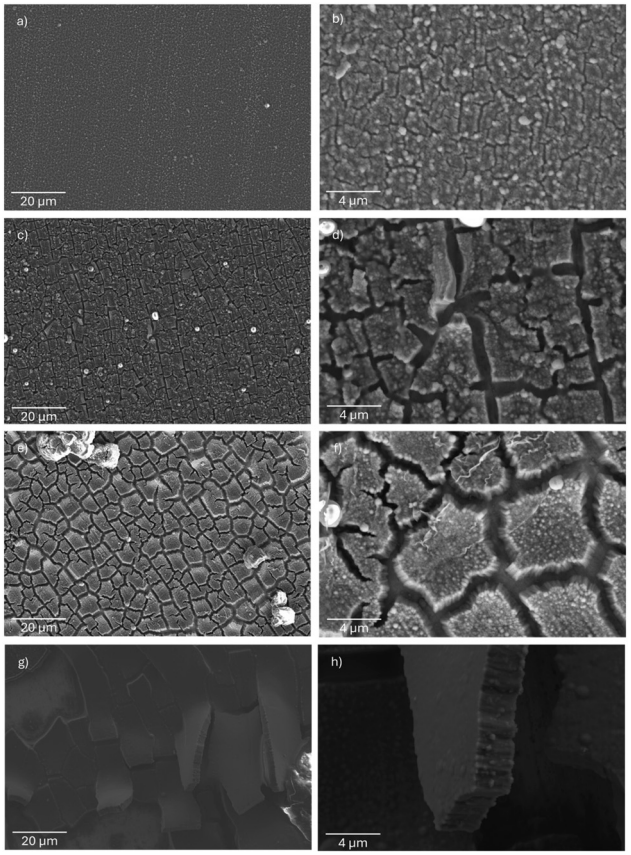

Fig. 7 Top-view SEM images of Si films deposited on Cu substrates with different Si thicknesses and magnifications. (a) 1000× and (b) 5000× magnification of 200 nm Si@Cu, (c) 1000× and (d) 5000× magnification of 500 nm Si@Cu, (e) 1000× and (f) 5000× magnification of 1000 nm Si@Cu and (g) 1000× and (h) 5000× magnification of 2000 nm Si@Cu. All images show post-mortem half cells that were disassembled after 50 galvanostatic cycles at C/20. The micrographs document the surface morphology of the Si layers after electrochemical cycling.

identified in SEM analysis. At these thicknesses, the films clearly exceed the critical thickness for mechanical stability, leading to stress relaxation predominantly through fracture and interfacial failure. These observations are consistent with previous reports on thick silicon thin films subjected to repeated lithiation-induced volume changes.[53,54,57] Overall, the post-mortem analysis provides direct visual confirmation that mechanical degradation and loss of adhesion dominate the failure behaviour at large silicon thicknesses.

Top-view SEM images taken after cycling (see Fig. 7) provide insight into the microstructural degradation mechanisms underlying the macroscopic behaviour observed in Fig. 6. For the 200 nm Si@Cu electrode, the surface morphology remains comparatively fine and homogeneous at 1000× and 5000× magnification. Only small, discontinuous cracks and moderate surface roughening are visible. This suggests that despite repeated lithiation and delithiation, the film largely retains its integrity and stress is accommodated without extensive fracturing. The electrochemical signatures indicate stable cycling after formation, these observations imply that the electrode primarily operates within the amorphous Li_xSi regime, thus avoiding mechanically destructive phase transformations.[18,58,59] After cycling, the 500 nm Si@Cu electrode exhibits a markedly roughened surface, with a clear network of microcracks and segmented domains visible at both magnifications. Such morphologies are characteristic of stress-driven fracture in lithiated silicon thin films, reflecting the transition from a dense, coherent film to a segmented structure that accommodates stress through controlled cracking.[48,54,56] Notably, the crack network remains relatively fine and interconnected. This explains why a significant proportion of the silicon remains electrochemically accessible, which is consistent with the high reversible capacities observed. Similar crack morphologies and their limited impact on electrochemical performance have been reported for silicon films close to their critical thickness.[48,54] Post-mortem SEM images of the 1000 nm Si@Cu electrode reveal a dense network of polygonal cracks with wide openings and clearly separated domains. This morphology indicates advanced mechanical degradation and extensive stress relaxation through fracture and segmentation. The size and separation of the domains suggest that significant portions of the silicon layer have become mechanically and electrically isolated from the current collector. This is consistent with the rapid capacity decay observed electrochemically. Such crack patterns are common in thick lithiated silicon films and are linked to stress localisation, interfacial debonding and the progressive loss of electrochemically active material.[53,54,56] The post-mortem morphology of the 2000 nm Si@Cu electrode differs fundamentally from the crack-dominated structures observed at lower thicknesses. Rather than a dense polygonal crack network, large, continuous domains with comparatively smooth surfaces are evident, alongside pronounced height variations and localised structural collapse. High-magnification images reveal features indicative of severe interfacial failure, including delamination and the formation of deep cavities or detached regions. This morphology suggests that the film exceeds the critical thickness at which stress can be accommodated by distributed cracking. Instead, mechanical degradation is dominated by interfacial debonding and subsequent buckling or spallation of the silicon layer. The presence of large detached regions implies that significant portions of the active material lose electrical contact with the current collector. This transition from crack-mediated stress relaxation to delamination-driven failure explains the drastic deterioration in electrochemical performance observed in the thickest films.

Taken together, the post-mortem optical and SEM analyses reinforce the conclusions drawn from the structural, morphological and electrochemical investigations. While increasing silicon thickness enhances the initial capacity, it also leads to a progressive change in the dominant degradation mechanism. Thin to intermediate films accommodate stress primarily through distributed crack

formation, which allows a substantial fraction of the active material to remain electrochemically accessible. In contrast, at large thicknesses, a transition to delamination-driven failure is observed, characterized by interfacial debonding, buckling and the formation of extended detached regions. This transition indicates the existence of a critical thickness above which stress can no longer be effectively dissipated by crack formation alone. Beyond this point, mechanical degradation results in large-scale electrical isolation of the silicon layer and a rapid loss of capacity. Consequently, an optimal thickness range exists for sputtered silicon anodes on copper, in which sufficient active material is present while mechanically destructive processes such as excessive fracture and delamination remain limited.

4. Conclusions

This study investigates the performance of magnetron-sputtered silicon thin films with thicknesses ranging from 200 to 2000 nm on copper current collectors. These are used as model anodes in soft solid-state lithium batteries. A combination of structural, morphological, electrochemical and post-mortem analyses was employed to elucidate the performance and degradation mechanisms of Si@Cu electrodes as a function of thickness. XRD confirmed that all deposited silicon layers were predominantly amorphous, while SEM revealed a transition from dense, compact growth at low thicknesses to columnar, stress-dominated growth at higher thicknesses. Electrochemical half-cell measurements revealed a pronounced non-monotonic relationship between reversible capacity and cycling stability, as well as silicon thickness. Thin 200 nm films exhibited high mechanical integrity and stable cycling but limited capacity. In contrast, 1000 nm and 2000 nm films displayed high initial capacities, which faded rapidly. A silicon thickness of 500 nm provided the most favourable balance between reversible capacity and cycling stability. Post-mortem analyses directly linked electrochemical performance to thickness-dependent mechanical degradation. Thin films largely retained adhesion to the copper substrate, while films of intermediate thickness showed controlled crack formation and segmentation that still permitted electrochemical accessibility. By contrast, thicker films exhibited extensive cracking, followed by interfacial debonding and partial delamination. This resulted in the active material becoming electrically isolated on a large scale. These observations suggest that, as film thickness increases, there is a transition from crack-mediated stress relaxation to delamination-driven failure.

The results also suggest that the polymer electrolyte and the silicon anode work together to govern interfacial stability. Although the mechanically compliant polymer electrolyte facilitates good initial contact and partially accommodates the volumetric changes of silicon due to its low stiffness and moderate ionic conductivity at elevated temperatures, it does not fully mitigate stress accumulation or mechanically induced degradation in thicker films. Consequently, interfacial degradation and contact loss remain strongly thickness-dependent, even in a soft solid-state configuration. The electrochemical performance of sputtered silicon anodes in soft solid-state batteries is therefore determined by the interplay of film thickness, growth morphology, chemomechanical stress evolution and interfacial stability, including the mechanical response of the polymer electrolyte. Therefore, active material loading alone is insufficient to ensure stable electrochemical performance in this system and careful control of silicon thickness within an appropriate range is required to achieve a balanced combination of reversible capacity and cycling stability. A systematic investigation of externally applied pressure therefore represents a logical next step to further elucidate the interplay between mechanical constraint, interfacial impedance and long-term stability.

Conflicts of interest

There are no conflicts to declare.

Data availability

The data that support the findings of this study are available within the article.

Supplementary information (SI) is available. See DOI: https://doi.org/10.1039/d6lf00035e.

Acknowledgements

This publication was funded by a joint matching funds initiative by Taiwan Tech (National Taiwan University of Science and Technology) and TU Braunschweig and by the German Federal Ministry of Research, Technology and Space with the project BiSSFest (03XP0412F).

Notes and references

1 L. Xu, S. Tang, Y. Cheng, K. Wang, J. Liang and C. Liu, *et al.*, Interfaces in Solid-State Lithium Batteries, *Joule*, 2018, **2**(10), 1991–2015.
2 Y. Xiao, Y. Wang, S.-H. Bo, J. C. Kim, L. J. Miara and G. Ceder, Understanding interface stability in solid-state batteries, *Nat. Rev. Mater.*, 2020, **5**(2), 105–126.
3 J. Janek and W. G. Zeier, A solid future for battery development, *Nat. Energy*, 2016, **1**(9), 16141.
4 X. Han, Y. Gong, K. Fu, X. He, G. T. Hitz and J. Dai, *et al.*, Negating interfacial impedance in garnet-based solid-state Li metal batteries, *Nat. Mater.*, 2017, **16**(5), 572–579.
5 Y. Zhu, X. He and Y. Mo, First principles study on electrochemical and chemical stability of solid electrolyte–electrode interfaces in all-solid-state Li-ion batteries, *J. Mater. Chem. A*, 2016, **4**(9), 3253–3266.
6 Y. Kato, S. Hori, T. Saito, K. Suzuki, M. Hirayama and A. Mitsui, *et al.*, High-power all-solid-state batteries using sulfide superionic conductors, *Nat. Energy*, 2016, **1**(4), 16030.
7 T. Asano, A. Sakai, S. Ouchi, M. Sakaida, A. Miyazaki and S. Hasegawa, Solid Halide Electrolytes with High Lithium-Ion

Conductivity for Application in 4 V Class Bulk-Type All-Solid-State Batteries, *Adv. Mater.*, 2018, **30**(44), e1803075.
8 Z. Xue, D. He and X. Xie, Poly(ethylene oxide)-based electrolytes for lithium-ion batteries, *J. Mater. Chem. A*, 2015, **3**(38), 19218–19253.
9 J. Mindemark, M. J. Lacey, T. Bowden and D. Brandell, Beyond PEO—Alternative host materials for Li + −conducting solid polymer electrolytes, *Prog. Polym. Sci.*, 2018, **81**, 114–143.
10 J. Janek and W. G. Zeier, Challenges in speeding up solid-state battery development, *Nat. Energy*, 2023, **8**(3), 230–240.
11 Z. Song, F. Chen, M. Martinez-Ibañez, W. Feng, M. Forsyth and Z. Zhou, *et al.*, A reflection on polymer electrolytes for solid-state lithium metal batteries, *Nat. Commun.*, 2023, **14**(1), 4884.
12 L. Porcarelli, A. S. Shaplov, F. Bella, J. R. Nair, D. Mecerreyes and C. Gerbaldi, Single-Ion Conducting Polymer Electrolytes for Lithium Metal Polymer Batteries that Operate at Ambient Temperature, *ACS Energy Lett.*, 2016, **1**(4), 678–682.
13 S. Tang, W. Guo and Y. Fu, Advances in Composite Polymer Electrolytes for Lithium Batteries and Beyond, *Adv. Energy Mater.*, 2021, **11**(2), 2000802.
14 F. Pei, L. Wu, Y. Zhang, Y. Liao, Q. Kang and Y. Han, *et al.*, Interfacial self-healing polymer electrolytes for long-cycle solid-state lithium-sulfur batteries, *Nat. Commun.*, 2024, **15**(1), 351.
15 A. Marinow, Z. Katcharava and W. H. Binder, Self-Healing Polymer Electrolytes for Next-Generation Lithium Batteries, *Polymers*, 2023, **15**(5), 1145.
16 M. N. Obrovac and V. L. Chevrier, Alloy negative electrodes for Li-ion batteries, *Chem. Rev.*, 2014, **114**(23), 11444–11502.
17 X. Zuo, J. Zhu, P. Müller-Buschbaum and Y.-J. Cheng, Silicon based lithium-ion battery anodes: A chronicle perspective review, *Nano Energy*, 2017, **31**, 113–143.
18 M. T. McDowell, S. W. Lee, J. T. Harris, B. A. Korgel, C. Wang and W. D. Nix, *et al.*, In situ TEM of two-phase lithiation of amorphous silicon nanospheres, *Nano Lett.*, 2013, **13**(2), 758–764.
19 T. Chen, J. Wu, Q. Zhang and X. Su, Recent advancement of SiOx based anodes for lithium-ion batteries, *J. Power Sources*, 2017, **363**, 126–144.
20 X. Fan, D. Deng, Y. Li and Q.-H. Wu, Recent Progress in SiC Nanostructures as Anode Materials for Lithium- Ion Batteries, *Curr. Mater. Sci.*, 2023, **16**(1), 18–29.
21 S. Cangaz, F. Hippauf, F. S. Reuter, S. Doerfler, T. Abendroth and H. Althues, *et al.*, Enabling High-Energy Solid-State Batteries with Stable Anode Interphase by the Use of Columnar Silicon Anodes, *Adv. Energy Mater.*, 2020, **10**(34), 267.
22 Y. Jin, B. Zhu, Z. Lu, N. Liu and J. Zhu, Challenges and Recent Progress in the Development of Si Anodes for Lithium-Ion Battery, *Adv. Energy Mater.*, 2017, **7**(23), 1700715.
23 R. Xu, L. Du, D. Adekoya, G. Zhang, S. Zhang and S. Sun, *et al.*, Well-Defined Nanostructures for Electrochemical Energy Conversion and Storage, *Adv. Energy Mater.*, 2021, **11**(15), 2001537.
24 H. Huo and J. Janek, Silicon as Emerging Anode in Solid-State Batteries, *ACS Energy Lett.*, 2022, **7**(11), 4005–4016.
25 M. Je, D.-Y. Han, J. Ryu and S. Park, Constructing Pure Si Anodes for Advanced Lithium Batteries, *Acc. Chem. Res.*, 2023, **56**(16), 2213–2224.
26 Z. Feng, W. Peng, Z. Wang, H. Guo, X. Li and G. Yan, *et al.*, Review of silicon-based alloys for lithium-ion battery anodes, *Int. J. Miner., Metall. Mater.*, 2021, **28**(10), 1549–1564.
27 T. K. Adhila, H. Elangovan, S. John, K. Chattopadhyay and H. C. Barshilia, Engineering the Microstructure of Silicon Nanowires by Controlling the Shape of the Metal Catalyst and Composition of the Etchant in a Two-Step MACE Process: An In-Depth Analysis of the Growth Mechanism, *Langmuir*, 2020, **36**(32), 9388–9398.
28 A. Mukanova, A. Jetybayeva, S.-T. Myung, S.-S. Kim and Z. Bakenov, A mini-review on the development of Si-based thin film anodes for Li-ion batteries, *Mater. Today Energy*, 2018, **9**, 49–66.
29 S.-Y. Ham, E. Sebti, A. Cronk, T. Pennebaker, G. Deysher and Y.-T. Chen, *et al.*, Overcoming low initial coulombic efficiencies of Si anodes through prelithiation in all-solid-state batteries, *Nat. Commun.*, 2024, **15**(1), 2991.
30 E. Adhitama, F. Dias Brandao, I. Dienwiebel, M. M. Bela, A. Javed and L. Haneke, *et al.*, Pre-Lithiation of Silicon Anodes by Thermal Evaporation of Lithium for Boosting the Energy Density of Lithium Ion Cells, *Adv. Funct. Mater.*, 2022, **32**(22), 2201455.
31 N. Dilger, M. Kaminski, J. Brokmann, J. Janssen, T. Neubert and S. Zellmer, Potentials of Magnetron Sputtering for Battery Applications—A Case Study for Thin Lithium Metal Anodes, *Surfaces*, 2026, **9**(1), 10.
32 F.-M. Wang, C.-C. Hu, S.-C. Lo, Y.-Y. Wang and C.-C. Wan, Definition of ionic transfer mechanisms based on positron annihilation studies in lithium batteries, *J. Electroanal. Chem.*, 2010, **644**(1), 25–29.
33 F.-M. Wang, C.-C. Hu, S.-C. Lo, Y.-Y. Wang and C.-C. Wan, The investigation of electrochemical properties and ionic motion of functionalized copolymer electrolytes based on polysiloxane, *Solid State Ionics*, 2009, **180**(4–5), 405–411.
34 F.-M. Wang, D.-T. Shieh, J.-H. Cheng and C.-R. Yang, An investigation of the salt dissociation effects on solid electrolyte interface (SEI) formation using linear carbonate-based electrolytes in lithium ion batteries, *Solid State Ionics*, 2010, **180**(40), 1660–1666.
35 F.-M. Wang, C.-C. Wan and Y.-Y. Wang, Synthesis of functionalized copolymer electrolytes based on polysiloxane and analysis of their conductivity, *J. Appl. Electrochem.*, 2009, **39**(2), 253–260.
36 J. A. Thornton, Influence of apparatus geometry and deposition conditions on the structure and topography of thick sputtered coatings, *J. Vac. Sci. Technol.*, 1974, **11**(4), 666–670.
37 H. Windischmann, Intrinsic stress in sputter-deposited thin films, *Crit. Rev. Solid State Mater. Sci.*, 1992, **17**(6), 547–596.
38 S. Roorda, W. C. Sinke, J. M. Poate, D. C. Jacobson, S. Dierker and B. S. Dennis, *et al.*, Structural relaxation and

defect annihilation in pure amorphous silicon, *Phys. Rev. B: Condens. Matter*, 1991, **44**(8), 3702–3725.
39 M. Armand and J.-M. Tarascon, Building better batteries, *Nature*, 2008, **451**(7179), 652–657.
40 D. T. Hallinan and N. P. Balsara, Polymer Electrolytes, *Annu. Rev. Mater. Res.*, 2013, **43**(1), 503–525.
41 C. Zhang and V. Nicolosi, Graphene and MXene-based transparent conductive electrodes and supercapacitors, *Energy Storage Mater.*, 2019, **16**, 102–125.
42 M. J. Lee, J. Han, K. Lee, Y. J. Lee, B. G. Kim and K.-N. Jung, *et al.*, Elastomeric electrolytes for high-energy solid-state lithium batteries, *Nature*, 2022, **601**(7892), 217–222.
43 E. Evshchik, D. Novikov, A. Levchenko, S. Nefedkin, A. V. Shikhovtseva and O. V. Bushkova, *et al.*, Magnetron Sputtering Silicon Thin Film Electrodes for Lithium-Ion Batteries, *Int. J. Electrochem. Sci.*, 2018, **13**(3), 2860–2874.
44 Z. Ahmad and C.-D. Yeo, Contact Mechanics of Solid-State Batteries, *ChemRxiv*, 2025, preprint, DOI: 10.26434/chemrxiv-2025-4lh9q.
45 A. Banerjee, X. Wang, C. Fang, E. A. Wu and Y. S. Meng, Interfaces and Interphases in All-Solid-State Batteries with Inorganic Solid Electrolytes, *Chem. Rev.*, 2020, **120**(14), 6878–6933.
46 Y. Zhang, S. Chen, Y. Chen and L. Li, Functional polyethylene glycol-based solid electrolytes with enhanced interfacial compatibility for room-temperature lithium metal batteries, *Mater. Chem. Front.*, 2021, **5**(9), 3681–3691.
47 D. H. S. Tan, A. Banerjee, Z. Chen and Y. S. Meng, Author Correction: From nanoscale interface characterization to sustainable energy storage using all-solid-state batteries, *Nat. Nanotechnol.*, 2021, **16**(4), 479.
48 V. A. Sethuraman, M. J. Chon, M. Shimshak, V. Srinivasan and P. R. Guduru, In situ measurements of stress evolution in silicon thin films during electrochemical lithiation and delithiation, *J. Power Sources*, 2010, **195**(15), 5062–5066.
49 C. Sångeland, G. Hernández, D. Brandell, R. Younesi, M. Hahlin and J. Mindemark, Dissecting the Solid Polymer Electrolyte-Electrode Interface in the Vicinity of Electrochemical Stability Limits, *ACS Appl. Mater. Interfaces*, 2022, **14**(25), 28716–28728.
50 J. Yu, X. Sun, X. Shen, D. Zhang, Z. Xie and N. Guo, *et al.*, Stack pressure-A critical strategy and challenge in performance optimization of solid state batteries, *Energy Storage Mater.*, 2025, **76**, 104134.
51 M. Raić, K. Kvastek, L. Mikac, N. Baran and M. Ivanda, The Effects of Silicon Anode Thickness on the Electrochemical Performance of Li-Ion Batteries, *Batteries*, 2023, **9**(3), 173.
52 E. Feyzi, M. R. AK, X. Li, S. Deng, J. Nanda and K. Zaghib, A comprehensive review of silicon anodes for high-energy lithium-ion batteries: Challenges, latest developments, and perspectives, *Next Energy*, 2024, **5**, 100176.
53 D. S. M. Iaboni and M. N. Obrovac, Li 15 Si 4 Formation in Silicon Thin Film Negative Electrodes, *J. Electrochem. Soc.*, 2016, **163**(2), A255–A261.
54 H. B. Chew, B. Hou, X. Wang and S. Xia, Cracking mechanisms in lithiated silicon thin film electrodes, *Int. J. Solids Struct.*, 2014, **51**(23–24), 4176–4187.
55 J. H. Ryu, J. W. Kim, Y.-E. Sung and S. M. Oh, Failure Modes of Silicon Powder Negative Electrode in Lithium Secondary Batteries, *Electrochem. Solid-State Lett.*, 2004, **7**(10), A306.
56 X. H. Liu, L. Zhong, S. Huang, S. X. Mao, T. Zhu and J. Y. Huang, Size-dependent fracture of silicon nanoparticles during lithiation, *ACS Nano*, 2012, **6**(2), 1522–1531.
57 M. Pharr, K. Zhao, X. Wang, Z. Suo and J. J. Vlassak, Kinetics of initial lithiation of crystalline silicon electrodes of lithium-ion batteries, *Nano Lett.*, 2012, **12**(9), 5039–5047.
58 M. N. Obrovac and L. Christensen, Structural Changes in Silicon Anodes during Lithium Insertion/Extraction, *Electrochem. Solid-State Lett.*, 2004, **7**(5), A93.
59 T. D. Hatchard and J. R. Dahn, In Situ XRD and Electrochemical Study of the Reaction of Lithium with Amorphous Silicon, *J. Electrochem. Soc.*, 2004, **151**(6), A838.